Precisely doping the surface of tin-based electrocatalysts for improved CO_2 conversion to liquid chemicals

Thuy-Duong Nguyen-Phan [a,b,*], James E. Ellis [a,b], Anantha Venkataraman Nagarajan [a,b,c], Bret H. Howard [a], Giannis Mpourmpakis [a,b,c,*], Douglas R. Kauffman [a,**]

[a] National Energy Technology Laboratory, 626 Cochran Mill Road, Pittsburgh, PA 15236, USA
[b] NETL Support Contractor, 626 Cochran Mill Road, Pittsburgh, PA 15236, USA
[c] Department of Chemical and Petroleum Engineering, University of Pittsburgh, Pittsburgh, PA 15261, USA

ARTICLE INFO

ABSTRACT

Doping tin catalysts with sulfur can improve the electrochemical CO_2 conversion into formate/formic acid, but the lack of composition-dependent activity trends hinders further catalyst development. Here, we precisely controlled the composition of sulfur-doped Sn catalysts to show that sulfur doping only improves CO_2 conversion over a very narrow composition range, achieving maximum activity at 1.4 at% S. *In situ* Raman spectroscopy indicted working catalysts were in a primarily metallic state (*e.g.* S-Sn), and we achieved some of the highest reported partial current densities in both H-cell and full-cell electrolyzer configurations. Density-functional theory calculations predicted S atoms preferentially occupied the catalyst surface and improved CO_2 reduction by localizing charge density at the catalyst/intermediate interface, which stabilized the *OCOH intermediate and lowered the CO_2 conversion thermodynamic barrier. Our work quantifies the composition-dependent influence of S dopants on Sn-based CO_2 reduction catalysts and provides a pathway for maximizing their CO_2 conversion activity.

1. Introduction

Electrochemical CO_2 reduction (CO_2R) into renewable chemicals and fuels, such as CO, formic acid, methane, or ethylene, is a promising pathway toward recycling carbon emissions [1,2]. Formic acid, or formate if electrochemically produced in a buffered or alkaline electrolyte, is a versatile two-electron liquid product that can be formed with high Faradaic efficiency (FE) and has potential uses in fuel cells, agricultural, chemical, and pharmaceutical applications [3,4]. Formic acid produced *via* CO_2R has also been identified as an economically viable green hydrogen carrier that potentially reduces the challenges associated with compressing, transporting and storing gaseous hydrogen [4].

Tin-, bismuth-, and indium-based catalysts are known to convert CO_2 into formic acid/formate [5], and ongoing efforts have focused on tuning catalyst composition to improve current density, product selectivity, and durability. Doping sulfur into these catalysts has recently been shown to improve CO_2R activity and selectivity by producing unique reaction sites, modifying the electronic structure and electron transfer kinetics, and reducing the formation energy of *OCOH reaction intermediates [6–9]. However, the literature still lacks clear composition-dependent activity trends that are needed to further advance sulfur-doped tin-based catalysts. Wang et al. [6] and Zheng et al. [9] both reported that small amounts of sulfur dopants (<5%) could greatly improve the CO_2 conversion activity of Sn-based electrocatalysts. DFT calculations predicted a composition-dependent change in the Gibbs free energy for *OCOH intermediate formation and associated theoretical limiting potential [9], but the precise relationship between sulfur-dopant levels and catalyst performance remains largely unexplored from an experimental standpoint. This knowledge gap of how sulfur dopant concentration impacts the CO_2R activity of Sn-based electrocatalysts is crucial for maximizing system efficiency and realizing deployable technologies that operate at industrially-relevant current densities [10–12].

In this work, we experimentally quantified the composition-

---

* Corresponding authors at: National Energy Technology Laboratory, 626 Cochran Mill Road, Pittsburgh, PA 15236, USA.
** Corresponding author.
E-mail addresses: ThuyDuong.NguyenPhan@netl.doe.gov (T.-D. Nguyen-Phan), gmpourmp@pitt.edu (G. Mpourmpakis), Douglas.Kauffman@netl.doe.gov (D.R. Kauffman).

dependent role of sulfur dopants and demonstrated its beneficial influence on CO_2 conversion only occurs over a very narrow composition range. The best-in-class catalyst contained 1.4 at% S content and produced a maximum formate partial current density of 264 ± 7 mA cm^{-2} ($81 \pm 6\%$ formate FE) in an aqueous H-cell configuration that was approximately five times larger than the undoped catalyst (54 ± 1 mA cm^{-2}; $57 \pm 6\%$ FE). In a single-gap, full-cell electrolyzer device, the 1.4% S-Sn catalyst produced an acidified formic acid solution at a maximum partial current density of 474 mA cm^{-2} and 79% FE. These figures of merit represent some of the highest performance metrics reported to date for Sn-based catalysts, and the sulfur-doped catalysts also demonstrated multi-hour stability in both H-Cell and full-cell configurations. Density-functional theory (DFT) calculations revealed that dilute S heteroatoms lowered the thermodynamic formation barrier by increasing electron localization at the catalytic reactive interface and stabilizing the key *OCOH intermediate *via* strengthened frontier orbital overlap. Our study shows that careful control of dopant atom inclusion and quantifying composition *vs.* performance trends is critical for maximizing electrocatalytic CO_2 conversion at S-doped Sn-based electrocatalysts.

2. Experimental section

2.1. Synthesis of as-prepared S-doped SnO_2 nanoparticles (S-SnO_2 NPs)

As prepared S-SnO_2 NPs were synthesized through a thermal sulfurization process by grinding SnO_2 NPs (Sigma, ≤ 100 nm average particle size) and sulfur powder (Sigma, 99.5–100.5% puriss p.a. grade; precipitated) with an agate mortar and pestle followed by thermal annealing in flowing N_2 between 400 and 700 °C (Table S1). The principle of this solid-state method is similar to literature reports for sulfur containing materials [13,14]. The quartz tube was purged with N_2 (~100 sccm) for at least 15 min at room temperature to completely remove air, and the furnace was heated to the set annealing temperature with a 10 °C min^{-1} ramp rate and held at the final temperature for 3 h. The S content in the S-SnO_2 NPs was controlled between 0.8 and 4.5 at% by varying the initial SnO_2:S precursor ratio and calcination temperature (Table S1). Undoped NPs were also thermally annealed at 600 °C for 3 h under flowing N_2 in the absence of S powder. A fresh quartz boat and quartz tube were used during the thermal annealing of undoped samples to eliminate unintentional sulfur contamination.

2.2. Materials characterization

High-angle annular dark-field scanning transmission electron microscopy (HAADF-STEM), high-resolution transmission electron microscopy (HR-TEM), energy dispersive X-ray spectroscopy (EDX), and elemental mapping were carried out on a FEI Titan Themis G2 200 Probe Cs Corrected Scanning Transmission Electron Microscope operated at an accelerating voltage of 200 kV. The powder sample was suspended in ethanol, drop-cast onto a holey carbon supported Cu grid, and dried in air. X-ray photoelectron spectroscopy (XPS) was carried out on a PHI 5000 VersaProbe III scanning XPS microprobe (Physical Electronics, ULVAC-PHI Inc) with Al Kα (1486.6 eV) radiation source and a hemispherical analyzer. All the binding energies were internally calibrated to the surface adventitious hydrocarbon feature (C 1 s) at 284.6 eV. Other characterizations techniques, including SEM, XRD, UV-Vis-DRS, Raman, N_2 sorption, FT-IR, and electrochemical measurements are described in detail in the Supplementary Material.

2.3. Electrochemical CO_2 reduction in an H-cell

Aqueous electrochemical measurements were conducted using a BioLogic SP-300 potentiostat and a gas-tight, two-compartment H-cell separated by a Nafion 117 proton exchange membrane [12]. 2.8 mg of catalyst powder, 0.3 mg of Vulcan XC-72R carbon black (Cabot), and 40

µL of Nafion 117 solution (5 wt%, Sigma) were dispersed in 400 µL of methanol under sonication. Working electrodes were prepared by drop-casting the catalyst ink onto 10% polytetrafluoroethylene (PTFE) treated Toray carbon paper (TGP-H-60, 0.2 ± 0.05 mm thickness, Alfa Aesar). The mass loadings were kept at 9.0 ± 1.2 mg$_{ink}$ cm$_{geo}^{-2}$ (5.2 ± 0.7 mg$_{catalyst}$ cm$_{geo}^{-2}$). A Pt mesh and Ag/AgCl (saturated NaCl, BASi) were used as the counter and reference electrodes, respectively.

The 60 mL of aqueous 0.1 M $KHCO_3$ catholyte (99.99%, Sigma) was continuously fed with high-purity CO_2 (Butler Gas, 99.999%) at a flow rate of 20 mL min^{-1} (pH ~ 6.8) under vigorous stirring for at least 20 min prior to each test and during all the experiments. All applied potentials were reported against the RHE, and the uncompensated ohmic resistance obtained by electrochemical impedance spectroscopy was automatically corrected at 85% (iR-correction) using the instrument software. All the current densities in this work were normalized to the exposed geometric area of the catalyst (0.08 ± 0.02 cm^2).

Chronoamperometric (current *vs.* time) measurements were performed for 30 min at each applied potential between -0.6 V to -1.4 V *vs.* RHE, and the gas/liquid products were collected every 30 min. The multi-hour stability was also evaluated at constant geometric current density of 200 mA cm^{-2} and at a constant cathode potential of -1.2 V *vs.* RHE. The gas products were collected in Tedlar gas-tight bags (Supelco) and quantified using a PerkinElmer Clarus 600 gas chromatography (GC) [12]. Liquid products collected from the catholyte were filtered with 0.22 µm PTFE syringe filters and analyzed using a Shimadzu high-performance liquid chromatography (HPLC) equipped with refractive index and photodiode array detectors, Aminex HPX-87 H column (Bio-Rad), and 5 mmol aqueous H_2SO_4 mobile phase. The calculation of Faradaic efficiency (FE) and partial current density for each product is described in the Supplementary Material. The standard deviation was obtained from at least three independent experiments with freshly prepared electrodes.

2.4. Electrochemical CO_2 reduction measurement in 6 cm^2 full-cell electrolyzer

The catalyst ink was prepared by sonicating a mixture of 30 mg of catalyst powder, 30 mg of Vulcan XC-72R carbon black (CB), 5 mL of deionized water, 1.97 mL of isopropanol, and 530 µL of Nafion 117 solution (5 wt%) for 60 min. To prepare a GDE cathode, seven additions of 300 µL of the ink were drop-casted on a 20% PTFE-treated Toray GDE placed on an 80 °C hot plate. After catalyst deposition, the 2.5 cm × 2.5 cm cathode (loading of 3 mg$_{ink}$ cm^{-2} or 1.1 mg$_{catalyst}$ cm^{-2}) was annealed at 120 °C in Ar to increase adhesion and remove any leftover solvent. It should be noted that catalyst ink recipes were optimized for the specific testing configuration to sustain high FE, maximize partial current density, and minimize overpotentials. H-cell experiments required a higher catalyst-to-carbon ratio to converts CO_2 dissolved in aqueous electrolyte (~30 µM) and excess CB reduced the apparent FE by evolving H_2, while full-cell experiments using GDEs required a lower ratio to convert pure (100%) CO_2 gas at the catalyst/electrolyte interface.

A commercially-available, formic acid full-cell electrolyzer (Dioxide Materials) was assembled in a modified configuration with a 3 cm × 3 cm IrO_2-based GDE anode (Dioxide Materials), a N-324 Nafion-based cation exchange membrane (Chemours), a polycarbonate central flow chamber filled with quartz wool (1.6 mm thick), and a catalyst-containing GDE cathode (Fig. S1). This modified configuration differed from the as-received full cell configuration by removing the anion-exchange membrane at the cathode and replacing ion-exchange resin beads in the central chamber with quartz wool to minimize bubble formation in the catholyte flow field. Teflon gaskets were used as spacers. Two peristaltic pumps delivered deionized water to the anode chamber (6 mL min^{-1}) and aqueous 0.4 M K_2SO_4 catholyte to the central chamber (3.6 mL min^{-1}), respectively. Dry CO_2 (100 sccm) was fed to the cathode side and the cell was operated at room temperature for all

electrolyzer experiments using a SP-150 potentiostat (BioLogic) connected with a 10 A, 20 V booster (BioLogic). The cell resistance was $1 \pm 0.25 \, \Omega$ determined by impedance measurements.

For polarization curve experiments, the electrolyzer cell was ramped step-wise in 30 min increments from 50 mA cm^{-2} (300 mA total cell current) to 700 mA cm^{-2} (4.2 A total cell current). The liquid flow from the central chamber outlet along with gas flow from the cathode outlet were collected in a sealed 250 mL glass bottle with three-port lid. Gas products were directly quantified using an in-line Perkin Elmer Clarus 590 GC with thermal conductivity and flame ionization detectors after passing through a cold trap and a desiccant trap to remove humidity. The collected effluent catholyte was filtered, diluted with deionized water, and analyzed with a Shimadzu HPLC as described in Experimental Section 2.3. The calculation of FE and energy efficiency (EE) for each product is also shown in the Supplementary Material.

2.5. Computational methods

Initial structures for bulk SnO$_2$ (110) and β-Sn (200) were obtained from Materials Project [15]. SnO$_2$ (110) was chosen because this facet displays the highest stability [16,17], and the metallic Sn (200) facet was chosen based on our previous quasi *in situ* XRD [12] and current *in situ* Raman that indicated both SnO$_2$ and S-SnO$_2$ became reduced at CO$_2$R-relevant electrochemical potentials. Thus, all surface chemistries were investigated on these two surfaces [6,16].

Periodic DFT calculations were performed with the computational package CP$_2$K [18] using the Perdew-Burke-Ernzerhof (PBE) functional [19,20], double-ζ valence polarized (DZVP) basis sets and Goedecker, Teter, and Hutter (GTH) pseudopotentials [21]. Grimme's D3 dispersion correction was used to account for long range interactions [22]. A convergence criterion of 0.02 eV/ Å along with an SCF and kinetic cut-off of 10^{-8} Ha and 500 Ry, respectively, was used for all geometry optimizations. A 4-layer model was chosen for geometry optimization of SnO$_2$ (110) surfaces, whereas a 5-layer model was chosen for Sn (200). For all surfaces, the first two layers were relaxed, and the rest of the layers were frozen during geometry optimization at their bulk positions. A vacuum of 20 Å in the z direction (vertical to the surface) was used to ensure enough spacing between the periodic images and prevent any interactions between images. The Gibbs free energies were calculated according to Equation (1): $\Delta G = \Delta E + \Delta ZPE + \int C_p dT - T\Delta S$, where E represents the ground state electronic energy, ZPE is the Zero Point Energy, C$_p$dT is the enthalpic correction, and S is the entropy. The vibrational modes of only the adsorbates and isolated molecules were considered to calculate G. To obtain more accurate energetics for the CO$_2$R pathway, gas phase corrections were used for the CO$_{2(g)}$ and H$_{2(g)}$ molecules [23] along with a correction to account for the liquid phase of HCOOH$_{(l)}$ [24]. The computational hydrogen electrode (CHE) [25] was utilized to account for the free energy associated with proton coupled electron transfer (PCET). The CHE equates the free energy of PCET as the free energy of ½ H$_{2(g)}$ molecule. This approach has been widely utilized and accurately captures experimentally determined trends of electrocatalytic reactions [26,27].

Various concentrations of S were considered (1.4%, 2.8%, 5.6%, 8.2% and 11.11%) for the slab models to obtain the optimal concentration of S doping on the surface. This consideration also allowed for identification of the threshold at which sulfur formed clusters on the surface. The aggregation energy (E_{seg}) of sulfur from the bulk to the surface of SnO$_2$ was investigated using Equation (2): $E_{seg} = (E_{undoped \, bulk} + E_{dopant \, on \, surface}) - (E_{dopant \, in \, bulk} + E_{undoped \, surface})$ [28]. A negative E_{seg} denotes that sulfur would prefer to segregate to the surface, whereas a positive E_{seg} denotes preference in the bulk.

3. Results & discussion

3.1. Materials synthesis and characterizations

The as-prepared electrocatalysts were synthesized in an oxide form. S-doped SnO$_2$ nanoparticles (S-SnO$_2$ NPs) were synthesized using a solid-state method where thermal vaporization of sulfur powder under inert atmosphere partially sulfurized the SnO$_2$ NPs. Due to low melting and boiling points of the sulfur powder precursor, calcination under flowing N$_2$ allowed the vaporized S atoms to diffuse into the SnO$_2$ NPs. The concentration of S atoms in the S-SnO$_2$ NPs was controlled between 0.8% and 4.5% (total atomic %, determined by XPS) by varying the sulfur-to-SnO$_2$ precursor ratio and calcination temperature (Table S1). S content above 4.5% led to the aggregation of sulfur on the NP surface and reduced CO$_2$R performance (*vide-infra*). Undoped SnO$_2$ NPs were also calcined under inert atmosphere in the absence of S to ensure equivalent thermal treatment as S-SnO$_2$ samples.

The as-prepared S-SnO$_2$ NP powders experienced an obvious color change compared with undoped SnO$_2$ NPs (Fig. 1a) and UV-Visible diffuse reflectance spectroscopy showed that S incorporation modified the SnO$_2$ spectral profile (Fig. S2). All S-SnO$_2$ NP and undoped SnO$_2$ NP samples demonstrated similar particle morphology with a heterogeneous particle size distribution (Figs. S3, S4), and the data in Table S1 show all samples had equivalent X-ray powder diffraction (XRD) crystallite sizes of 30 ± 1 nm and Brunauer–Emmett–Teller (BET) surface areas of 19 ± 3 m^2 g^{-1}.

Representative high-angle annular dark-field scanning transmission electron microscopy (HAADF-STEM), energy dispersive X-ray spectroscopy (EDX), and corresponding elemental mapping images of a 1.4% S-SnO$_2$ (composition by XPS) indicated uniformly distributed S atoms across the NP surface (Figs. 1b, c). XRD and Raman spectroscopy confirmed that all S-SnO$_2$ NPs and undoped SnO$_2$ NPs retained the parent tetragonal SnO$_2$ structure with no evidence of bulk elemental sulfur, SnS, or SnS$_2$ compounds (Fig. 1d and Fig. S5). XPS analysis of the 1.4% S-SnO$_2$ NPs identified a unique S 2p peak shape compared with SnS and SnS$_2$ (Fig. 1e) and modification to the near-Fermi region of the valence band (VB) (Fig. 1f).

Interestingly, the total atomic S content determined from XPS (1.4%) was much higher than determined from HAADF-STEM/EDX and SEM/EDX (0.2–0.25%). Considering the probe depth differences between XPS (few nm) and EDX (~100 s nm) [29,30], equivalent XPS and EDX determined compositions would indicate a homogeneous S distribution through the entire particle volume. Our observation of a substantially higher XPS-determined S content suggests preferential incorporation of S atoms in the near-surface region of the S-SnO$_2$ NPs. However, 4.5% S-SnO$_2$ NPs (by XPS) demonstrated a S 2p doublet that resembled elemental sulfur [31,32] and/or polysulfide species [31,33], along with FTIR [34] and Raman [35] signatures characteristic of surface -SO$_x$ species. This observation suggests potential surface aggregation of S atoms or the formation of small sulfur clusters at higher S content (Fig. S5).

DFT was utilized to understand S incorporation into SnO$_2$ (Fig. 1g). We considered the most stable (110) facet [16,17] that contained bi-coordinated bridging oxygen atoms (O$_b$) and tetracoordinated in-plane oxygen atoms (O$_p$). The S-SnO$_2$ structure included a single surface S atom (approximately one S atom/9 nm^2) and a total S content of ~1.4% within the first four SnO$_2$ layers to represent the near-surface region of the experimentally prepared 1.4% S-SnO$_2$ NPs. Thermodynamic analysis revealed preferential S occupation at the bridging O$_b$ site that was 0.33 eV more favorable than in-plane O$_p$ sites. Notably, increasing the S concentration from 1.4% S to 11.1% S led to S aggregation and the formation of small sulfur clusters (Fig. S6), which is qualitatively consistent with our experimental observation of surface S species in the 4.5% S-SnO$_2$ NPs. The dopant concentration depends on the unit-cell size, and the quantitative deviation between the S aggregation content in experiments *vs.* DFT is because XPS probes
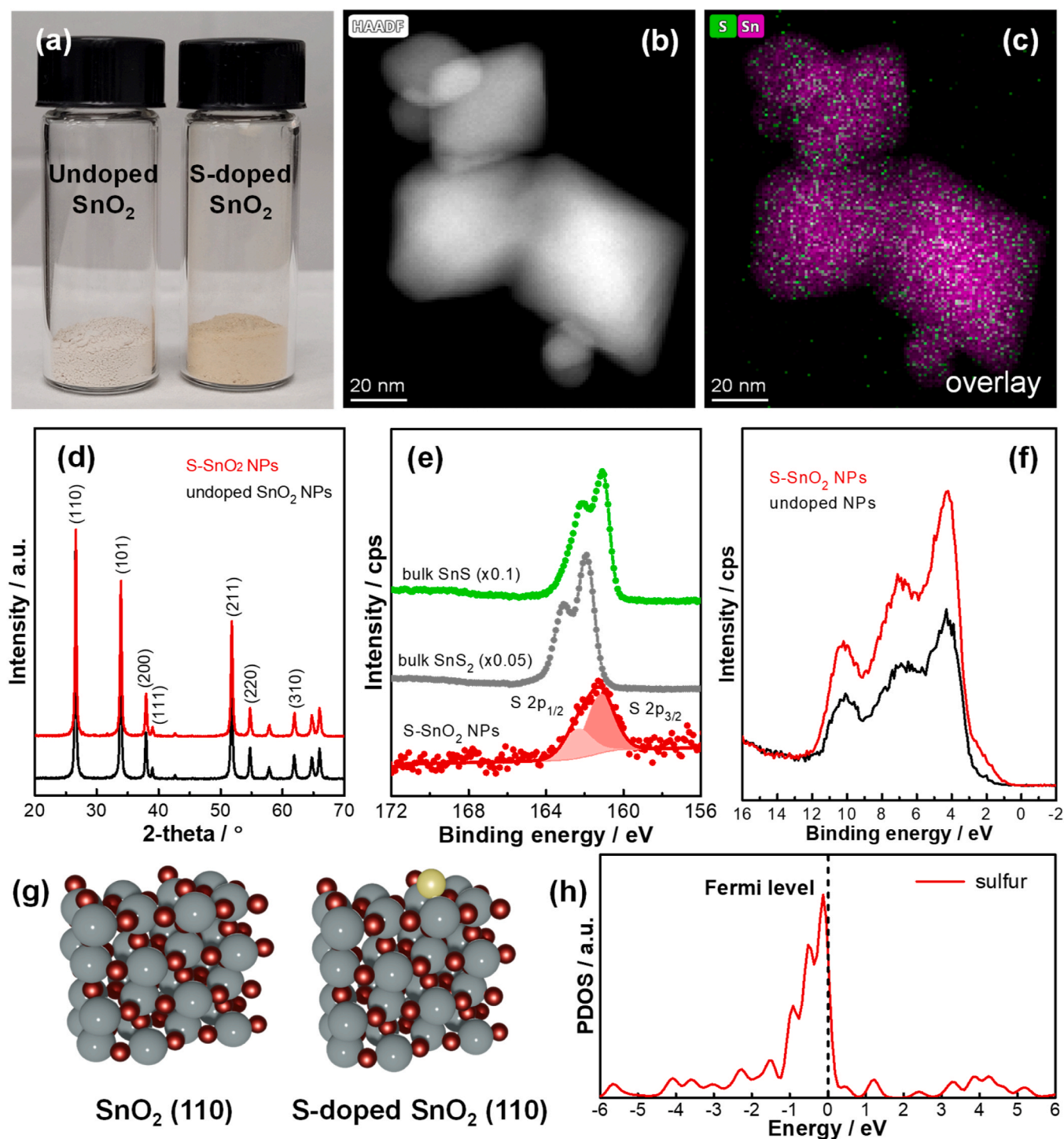
Fig. 1. (a) Picture of as-prepared SnO_2 NP and 1.4% $S-SnO_2$ NP samples. (b) HAADF-STEM image and (c) overlay EDX elemental mapping of 1.4% $S-SnO_2$ NPs. (d) XRD, (e) XPS S 2p spectra, and (f) XPS of the valence band region for undoped SnO_2 NPs and 1.4% $S-SnO_2$ NPs. (g) DFT-optimized structure of SnO_2 (110) and 1.4% $S-SnO_2$ (110) (grey: Sn, red: O, yellow: S). (h) Projected density of states (PDOS) of sulfur states in 1.4% $S-SnO_2$ (110) with the dotted line representing the Fermi level (0 eV). Note that the S 2p spectra of bulk SnS_2 and bulk SnS standards in panel (e) were included for XPS peak shape and binding energy comparison.

composition changes deeper in the oxide than what is practical to simulate with DFT in terms of computational cost (4-layer thick unit-cell). However, these results further point to preferential sulfur incorporation in the near-surface region and the possibility of sulfur surface aggregation at higher S content. The projected density of states (PDOS) shown in Fig. 1h predict S-centered states near the Fermi-level that are consistent with the new low-energy feature in the $S-SnO_2$ VB-XPS. Higher energy features between 4 and 12 eV in the

experimental VB XPS were assigned to a combination of O and Sn-centered states that were predicted to be relatively unaffected by S incorporation (Fig. S7).

3.2. Electrochemical CO_2 reduction in an aqueous H-cell

The *in situ* Raman spectroscopy results presented in Fig. S8 and previous *quasi in situ* XRD experiments [12] showed that the as-prepared

Sn-oxide materials can be reduced into a primarily metallic state at sufficiently large CO_2R overpotentials (*e.g.* −0.8 to −1.2 V *vs.* RHE), and we have termed our working catalysts (during CO_2R) as "Sn" and "S-Sn" hereafter. However, we cannot completely rule out that some fraction of the catalyst surface may retain thin oxide phases during CO_2R, as suggested in some literature reports [36,37].

We initially evaluated the CO_2R performance of Sn and S-Sn electrocatalysts in an H-cell containing CO_2 saturated 0.1 M $KHCO_3$. Formate was the primary product at larger overpotentials for all catalysts, whereas H_2 was dominant toward lower overpotentials (Figs. S9, S10). Figs. 2a, 2b show that 1.4% S-Sn NPs produced higher formate FE and formate partial current density ($j_{formate}$) than undoped Sn NPs over a wide potential window. The 1.4% S-Sn NPs achieved a maximum 88 ± 2% formate FE at − 1.2 V *vs.* reversible hydrogen electrode (RHE)
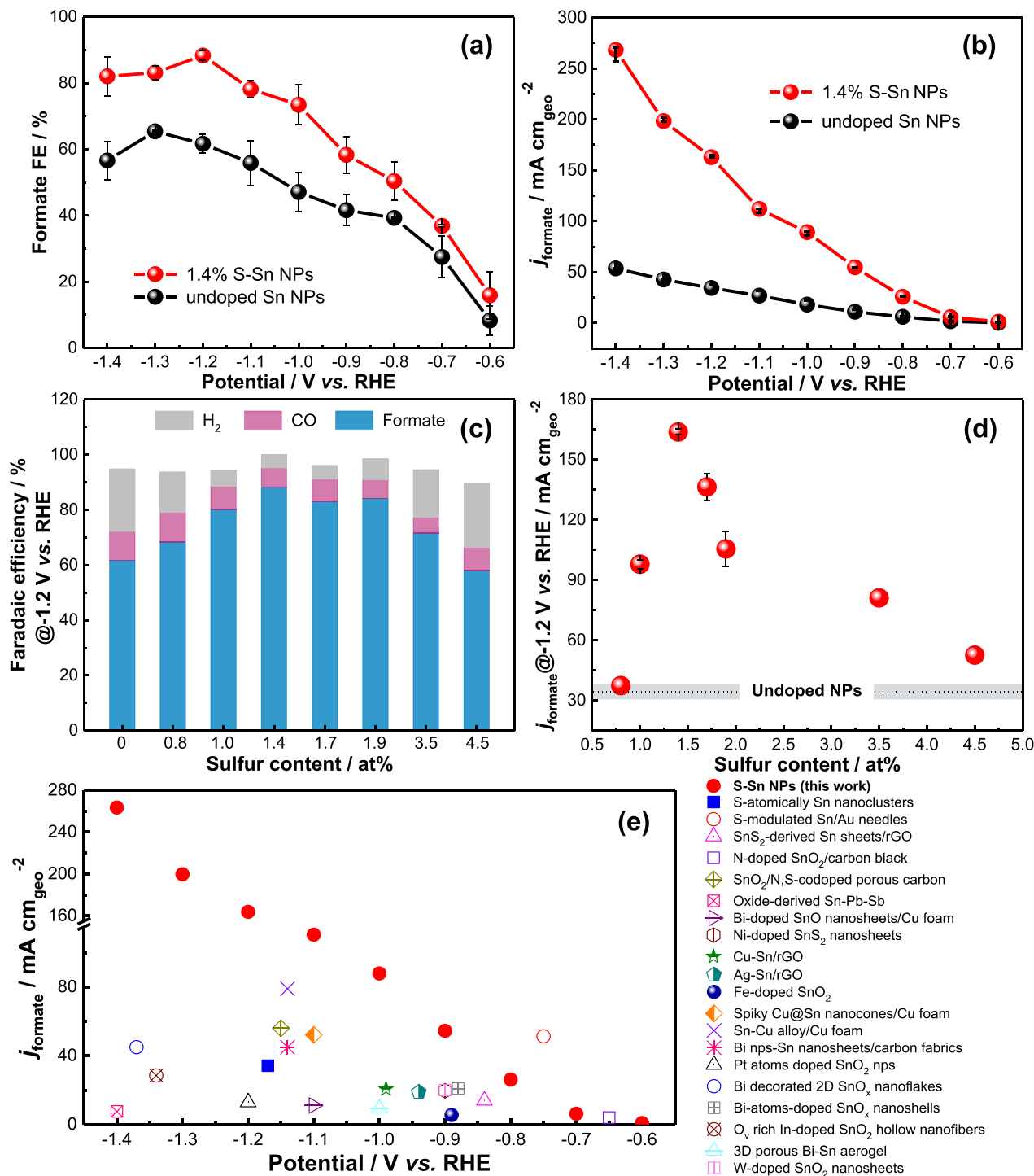
Fig. 2. CO_2R performance in CO_2-saturated 0.1 M $KHCO_3$ electrolyte in an aqueous H-cell. Potential dependent (a) formate FE and (b) formate partial current density ($j_{formate}$) of 1.4% S-Sn NPs and undoped Sn NPs. Composition-dependent (c) formate FE and (d) $j_{formate}$ of S-Sn NPs catalysts at -1.2 V *vs.* RHE (in panel d, the dashed line for undoped Sn NPs represents the average and the shaded gray area represents the standard deviation). (e) Comparison between $j_{formate}$ of 1.4% S-Sn NPs in this study and previously published Sn-based catalysts at cathode potentials that produced maximum formate FEs in an H-cell. *Note:* Specific details and references for the literature catalyst values in panel (e) are listed in Table S2.

with $j_{formate} = 164 \pm 2$ mA cm^{-2}, compared with 34 ± 4 mA cm^{-2} (62 $\pm$ 3% FE) for undoped Sn NPs at the same potential. At a larger over-potential (-1.4 V *vs* RHE), the 1.4% S-Sn produced $j_{formate} = 264 \pm 7$ mA cm^{-2} and 81 ± 6% formate FE that was approximately five times larger than undoped Sn NPs (54 ± 1 mA cm^{-2}; 57 ± 6% FE). The 1.4% S-Sn NPs also sustained $j_{formate}$ values between 150 and 160 mA cm^{-2} (75–80% FE) over several hours in both constant current and constant potential operational modes (Fig. S11). Post-reaction XPS analysis for 1.4%S-Sn NPs electrodes in Fig. S12 indicates the sustained S and the reduction of SnO$_2$ into lower oxidation states after several hours of operation. Note that oxide state could be presumably due to the reoxidation of metallic Sn (proved by *in situ* Raman analysis) after prolonged air exposure. Furthermore, post-reaction EDX mapping a control S-Sn electrode prepared with sulfur-free Sustainion ionomer binder and no carbon conducting material confirmed S remained in the catalyst after CO$_2$R (Fig. S13).

The 1.4% S-Sn NPs and undoped Sn NPs had similar electrochemical surface areas (~40 cm^2) and Tafel slopes (130–140 mV decade^{-1}) (Fig. S13). However, electrochemical impedance spectroscopy showed 1.4% S-Sn had smaller charge transfer resistance (R_{ct}) compared with undoped Sn NPs (Fig. S13). These results point to S dopant atoms as the origin of the improved CO$_2$R current density, rather than differences in particle surface area or CO$_2$R rate liming step.

Previous work has also shown S dopants can improve the CO$_2$R performance of Sn-based catalysts [6,9], but the precise relationship between sulfur content and catalyst activity has yet to be explored. This motivated us to quantify composition-dependent electrocatalytic activity, and Figs. 2c, 2d present the formate FE and $j_{formate}$ as a function of S content at a representative cathode potential of -1.2 V *vs.* RHE. The $j_{formate}$ increased rapidly over a narrow composition range and peaked at 1.4% S. Above this point, CO$_2$R performance slowly decreased as S content increased up to 4.5% S, which was the maximum doping-level investigated here due to apparent surface aggregation of sulfur atoms. Similar composition-dependent $j_{formate}$ trends were also observed between -0.8 V and -1.4 V *vs.* RHE and 1.4% S-Sn NPs were consistently the most active composition (Figs. S9 and S14).

Fig. 2e and Table S2 compare the H-cell performance of the 1.4% S-Sn NPs with other Sn-based catalysts reported in the literature (details and references listed in Table S2). The plotted literature values represent reported $j_{formate}$ values at the cathode potential that produced the highest formate FE. The results clearly show that 1.4% S-Sn NPs produced some of the highest reported $j_{formate}$ to date in an H-cell configuration.

3.3. Density functional theory calculations

We applied DFT calculations and the computational hydrogen electrode method [25] to analyze the CO$_2$R and hydrogen evolution reaction (HER) free energy pathways on undoped Sn (200) and sulfur-doped Sn (200). The Sn (200) orientation was chosen based on our previous *quasi in situ* XRD analysis of SnO$_2$ [12] and current *in situ* Raman results for S-SnO$_2$ (Fig. S8).

Electrochemical reduction of CO$_2$ into formate/formic acid proceeds through an oxygen-bound *OCOH intermediate [6,9,20,38,39], whereas CO formation proceeds through a carbon-bound *COOH intermediate [40]. Formation of the *COOH intermediate (and corresponding CO product) was predicted to be > 1 eV more endergonic than *OCOH formation at both catalysts (Fig. S15), which is consistent with the high formate FE observed in experiments. The CO$_2$R free energy pathways and optimized *OCOH binding configurations are shown in Fig. 3a. Bidentate *OCOH adsorption occurred at two Sn atoms on both Sn (200) and S-Sn (200), even if the starting structure was bound to one S atom and one Sn atom. We found a substantially reduced *OCOH formation energy (0.07 *vs.* 0.80 eV) at S-Sn (200) compared to undoped Sn (200) that resulted in a 0.29 eV smaller predicted CO$_2$R limiting potential (U$_{L, CO2R}$). All DFT results are summarized in Table S3.
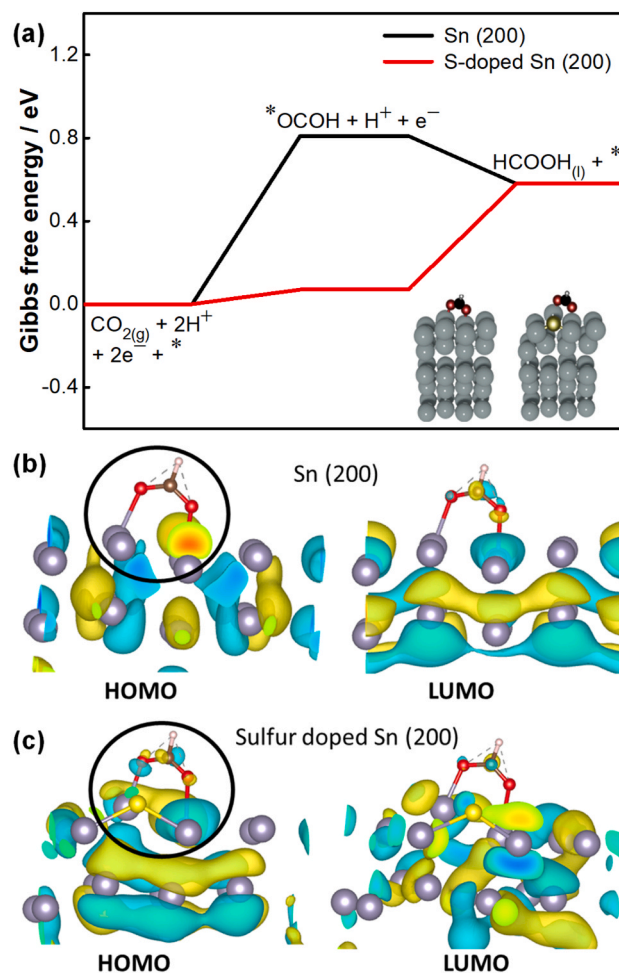
Fig. 3. (a) CO$_2$R pathway on Sn (200) and sulfur-doped Sn (200). Inset depicts optimized configurations of the *OCOH intermediate on Sn (200) and S-doped Sn (200). *Colors*: grey Sn, red O, yellow S, white H, black C. (b, c) The highest occupied molecular orbital (HOMO) and lowest unoccupied molecular orbital (LUMO) of Sn (200) and S-doped Sn (200) when *OCOH is adsorbed on Sn active sites. Green and yellow demonstrate charge densities (negative and positive wavefunctions, respectively).

The reduced *OCOH formation energy between the S-Sn (200) and Sn (200) surfaces can be explained by examining the highest occupied molecular orbital (HOMO) and the lowest unoccupied molecular orbital (LUMO) upon *OCOH adsorption (Fig. 3b, c). Greater frontier orbital overlap between *OCOH (circled in black) and S-Sn (200) compared with undoped Sn (200) implies increased electronic interaction and greater *OCOH stabilization at S-Sn (200). The sulfur dopant on the S-Sn (200) surface also increased electron density localization at the *OCOH—Sn interface, which suggests improved charge transfer under reaction conditions [7] and supports experimental observations of lower R_{ct} for the 1.4% S-Sn catalysts (Fig. S13).

Notably, H* formation barriers at Sn active sites were > 0.4 eV more endergonic than *OCOH formation at both catalysts, and the predicted U$_{L,HER}$ values were larger than U$_{L,CO2R}$ (Fig. S16 and Table S3). This result qualitatively predicts CO$_2$R selectivity for both catalysts and the lower U$_{L,CO2R}$ associated with S-Sn (200) suggests that it should produce higher $j_{formate}$ than Sn (200) at relevant overpotentials, which agrees with experimental results. We also found lower U$_{L,CO2R}$ for an oxidized S-doped SnO$_2$ (110) surface compared with undoped SnO$_2$ (110) (Fig. S17), suggesting S-doping still improves catalytic activity even if some fraction of the catalyst surface retained an oxide phase during CO$_2$R. Taken together, the DFT results predict that the more

thermodynamically favorable *OCOH *vs.* *H formation, coupled with better *OCOH stabilization and increased electron localization at the intermediate/catalyst interface, could help S-Sn (200) sustain higher $j_{formate}$ than undoped Sn (200) at experimentally relevant overpotentials.

## 3.4. Electrochemical CO₂ reduction in a full-cell electrolyzer device

Finally, we evaluated the performance of the 1.4% S-Sn and undoped Sn NP catalysts in a single-gap, full-cell electrolyzer to compare performance differences in a more realistic device architecture that can achieve industrially-relevant current densities exceeding 100 mA cm^{-2} [10]. The cell design is described in the **Experimental Section** and shown in **Fig. S1**. Notably, proton transport through the Nafion cation exchange membrane during electrolyzer operation acidified the initially neutral, unbuffered catholyte and resulted in an effluent formic acid (rather than formate) product stream with bulk pH values between 2 and 3 (**Fig. S18**). This low-pH catholyte scenario should also help mitigate carbonate/bicarbonate formation at the cathode and may facilitate down-stream formic acid concentration/purification compared with formate production in basic or neutral-buffered catholytes [41,42].

Full-cell polarization data in **Fig. 4**a present the total current density, full-cell voltage, and formic acid FE using 1.4% S-Sn NPs as the cathode catalyst. In contrast to H-cell and other half-cell results that only consider the cathode potential against a reference electrode, the reported full-cell voltages include the sum of the cathode potential, anode

potential, and cell resistance contributions (*e.g.* catholyte resistance, membrane resistance, *etc.*). We observed a maximum formic acid partial current density (j_{HCOOH}) of 474 mA cm^{-2} and 79% FE at a cell voltage of 6.5 V. In comparison, undoped Sn NPs showed reduced performance with sharply decreased FE towards higher total current densities, larger full-cell voltages, and a smaller maximum j_{HCOOH} of 402 mA cm^{-2} (**Fig. S19**). The improved electrolyzer performance of 1.4% S-Sn NPs compared with undoped Sn NPs agrees well with both H-cell results and DFT findings. Moreover, the 1.4% S-Sn NPs sustained $j_{HCOOH} = 169 \pm 7$ mA cm^{-2} and $FE_{HCOOH} = 84 \pm 3\%$ during a 16-hour electrolysis at constant 200 mA cm^{-2} total applied current density that included several start/stop cycles with overnight holds at open circuit (**Fig. 4**b).

Fig. 4c and **Table S4** compares the full-cell electrolyzer performance of 1.4% S-Sn NPs and undoped Sn NPs catalysts from this work to other literature reports of Sn-based catalysts in full-cell devices (details and references listed in **Table S4**). The energy efficiency (EE) was calculated from the cell voltage required to achieve maximum j_{HCOOH}, and 1.4% S-Sn NPs are one of the highest performing catalysts with a combination of $j_{HCOOH} = 474$ mA cm^{-2} and an EE of 17.4%. Recent literature suggests low-temperature, single-gap electrolyzer devices may have an upper j_{HCOOH} limit of ~500 mA cm^{-2} [43], thus further reductions in catalyst overpotentials and cell resistances are future targets to improve high-current density EE in this cell design. Moreover, emerging cell designs, such as exsolution-induced CO₂ flow cells [43] or all-solid-state cells [44], may represent other opportunities to increase formic acid partial current density to the ampere level where the differences in
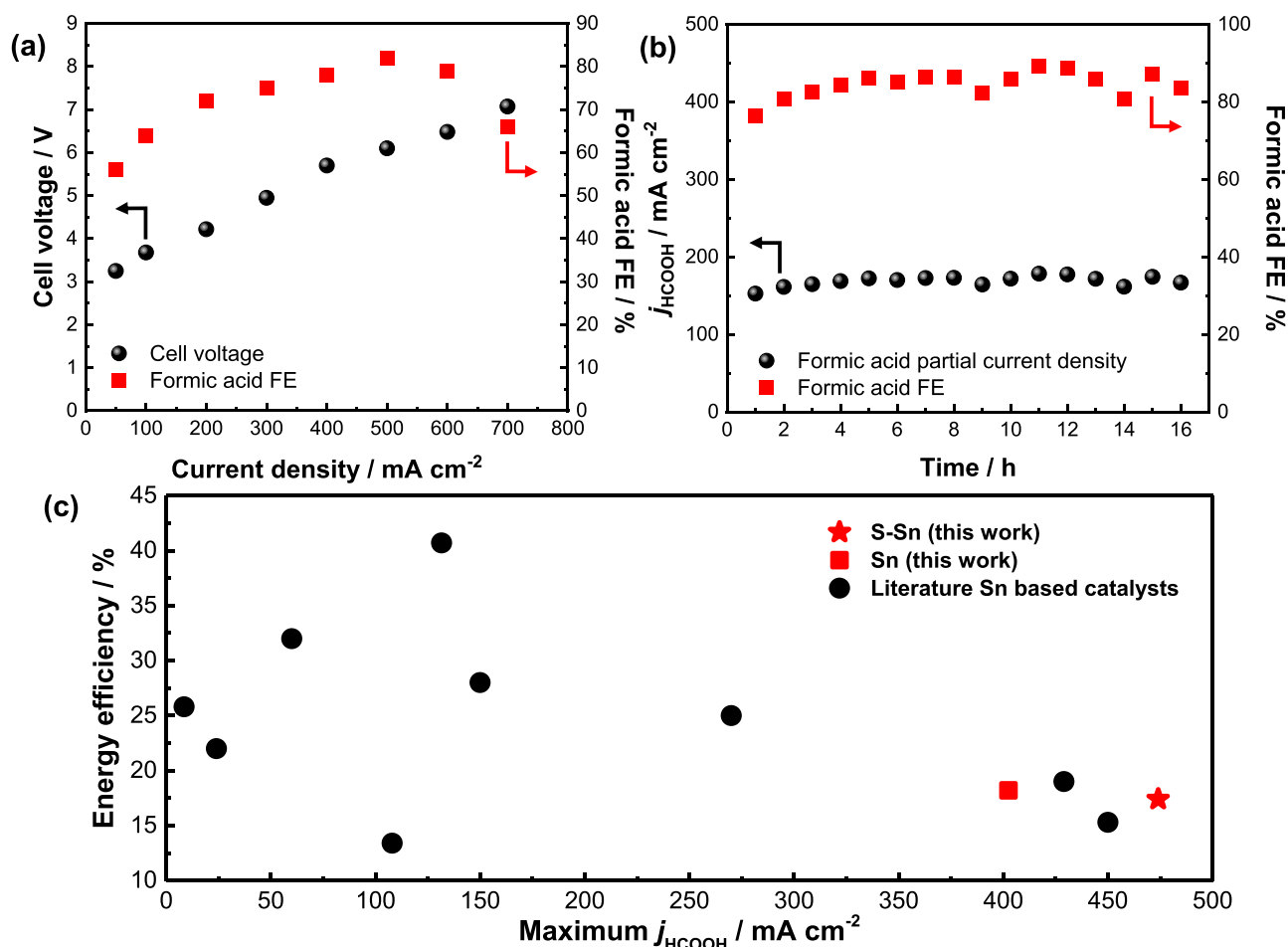
Fig. 4. CO₂R performance of 1.4% S-Sn in 6-cm², single-gap, full-cell electrolyzer. (a) Full-cell polarization curve of 1.4% S-Sn cathode showing cell voltage and formic acid FE *vs.* total current density. (b) Formic acid partial current density (j_{HCOOH}) and FE of 1.4% S-Sn over 16 h at an applied total current density of 200 mA cm^{-2}. (c) Comparison of energy efficiency at maximum j_{HCOOH} from this work *vs.* other literature-based Sn catalysts tested in full-cell electrolyzer configurations. *Note:* Specific details and references for the literature catalyst values in panel (c) are listed in listed in **Table S4**.

catalyst performance may become even more distinct [45].

4. Conclusion

Taken together, by combining precise catalyst synthesis and characterization, electrocatalytic studies, and DFT analysis, we fully resolved and optimized the composition-dependent CO_2R activity of S-doped Sn electrocatalysts. Incorporating precise amounts of S atoms into the near surface region of Sn NPs between 1 and 2 at% maximized CO_2 conversion to formate/formic acid. The best performing 1.4% S-Sn catalyst produced some of the highest partial current densities reported to date for H-cell ($j_{formate} = 264 \pm 7$ mA cm^{-2}) and full-cell devices ($j_{HCOOH} = 474$ mA cm^{-2}). Computational modeling additionally revealed the improved performance of S-Sn was due to S heteroatoms increasing key intermediate stabilization and reducing the limiting potential. This demonstration of how dilute S dopants beneficially impact CO_2 conversion in different cell configurations provides further insight into the design of high performance CO_2R electrocatalysts.

CRediT authorship contribution statement

T.-D. N.-P.: Conceptualization, Methodology, Investigation, Data curation, Formal analysis, Validation, Visualization, Writing – original draft. **J. E. E.:** Methodology, Investigation, Data curation, Formal analysis, Validation, Writing – original draft. **A. V. N.:** Methodology, Software, Investigation, Data curation, Formal analysis, Validation, Writing – original draft. **B. H. H.:** Investigation, Formal analysis, Writing – review & editing. **G. M.:** Resources, Data Curation, Supervision, Funding acquisition, Writing - Review & Editing. **D. R. K.:** Conceptualization, Resources, Data curation, Validation, Supervision, Project administration, Funding acquisition, Writing - Review & Editing.

Declaration of Competing Interest

The authors declare that they have no known competing financial interests or personal relationships that could have appeared to influence the work reported in this paper.

Data Availability

Data will be made available on request.

Acknowledgment

Disclaimer

Supplementary Material

Supplementary Experimental; Supplementary Tables S1-S4; Supplementary Figs. S1-S20.

Appendix A. Supporting information

Supplementary data associated with this article can be found in the online version at doi:10.1016/j.apcatb.2023.123250.

References

[1] S. Overa, B.H. Ko, Y. Zhao, F. Jiao, Electrochemical approaches for CO_2 conversion to chemicals: a journey toward practical applications, Acc. Chem. Res. 55 (2022) 638–648, https://doi.org/10.1021/acs.accounts.1c00674.

[2] P. Prabhu, V. Jose, J.-M. Lee, Heterostructured catalysts for electrocatalytic and photocatalytic carbon dioxide reduction, Adv. Funct. Mater. 30 (2020), 1910768, https://doi.org/10.1002/adfm.201910768.

[3] X. Chen, Y. Liu, J. Wu, Sustainable production of formic acid from biomass and carbon dioxide, Mol. Catal. 483 (2020), 110716, https://doi.org/10.1016/j.mcat.2019.110716.

[4] B.S. Crandall, T. Brix, R.S. Weber, F. Jiao, Techno-economic assessment of green H2 carrier supply chains, Energy Fuels (2022), https://doi.org/10.1021/acs.energyfuels.2c03616.

[5] N. Han, P. Ding, L. He, Y. Li, Y. Li, Promises of main group metal–based nanostructured materials for electrochemical CO_2 reduction to formate, Adv. Energy Mater. 10 (2020), 1902338, https://doi.org/10.1002/aenm.201902338.

[6] X. Wang, F. Li, W.-J. Yin, Y. Si, M. Miao, X. Wang, Y. Fu, Atomically dispersed sn modified with trace sulfur species derived from organosulfide complex for electroreduction of CO_2, Appl. Catal. B Environ. 304 (2022), 120936, https://doi.org/10.1016/j.apcatb.2021.120936.

[7] S.-Q. Liu, M.-R. Gao, R.-F. Feng, L. Gong, H. Zeng, J.-L. Luo, Electronic delocalization of bismuth oxide induced by sulfur doping for efficient CO_2 electroreduction to formate, ACS Catal. 11 (2021) 7604–7612, https://doi.org/10.1021/acscatal.1c01899.

[8] W. Ma, S. Xie, X.-G. Zhang, F. Sun, J. Kang, Z. Jiang, Q. Zhang, D.-Y. Wu, Y. Wang, Promoting electrocatalytic CO_2 reduction to formate via sulfur-boosting water activation on indium surfaces, Nat. Commun. 10 (2019) 892, https://doi.org/10.1038/s41467-019-08805-x.

[9] X. Zheng, P. De Luna, F.P. García de Arquer, B. Zhang, N. Becknell, M.B. Ross, Y. Li, M.N. Banis, Y. Li, M. Liu, O. Voznyy, C.T. Dinh, T. Zhuang, P. Stadler, Y. Cui, X. Du, P. Yang, E.H. Sargent, Sulfur-modulated tin sites enable highly selective electrochemical reduction of CO_2 to formate, Joule 1 (2017) 794–805, https://doi.org/10.1016/j.joule.2017.09.014.

[10] R.I. Masel, Z. Liu, H. Yang, J.J. Kaczur, D. Carrillo, S. Ren, D. Salvatore, C.P. Berlinguette, An industrial perspective on catalysts for low-temperature CO_2 electrolysis, Nat. Nanotechnol. 16 (2021) 118–128, https://doi.org/10.1038/s41565-020-00823-x.

[11] Y. Chen, A. Vise, W.E. Klein, F.C. Cetinbas, D.J. Myers, W.A. Smith, T.G. Deutsch, K.C. Neyerlin, A. Robust, Scalable platform for the electrochemical conversion of CO_2 to formate: identifying pathways to higher energy efficiencies, ACS Energy Lett. 5 (2020) 1825–1833, https://doi.org/10.1021/acsenergylett.0c00860.

[12] T.-D. Nguyen-Phan, L. Hu, B.H. Howard, W. Xu, E. Stavitski, D. Leshchev, A. Rothenberger, K.C. Neyerlin, D.R. Kauffman, High current density electroreduction of CO_2 into formate with tin oxide nanospheres, Sci. Rep. 12 (2022) 8420, https://doi.org/10.1038/s41598-022-11890-6.

[13] H. Araki, Y. Kubo, A. Mikaduki, K. Jimbo, W.S. Maw, H. Katagiri, M. Yamazaki, K. Oishi, A. Takeuchi, Preparation of Cu_2ZnSnS_4 thin films by sulfurizing electroplated precursors, Sol. Energy Mater. Sol. Cells 93 (2009) 996–999, https://doi.org/10.1016/j.solmat.2008.11.045.

[14] K. Zhang, Q. Zhao, Z. Tao, J. Chen, Composite oF Sulfur Impregnated in Porous Hollow Carbon Spheres as the Cathode of Li-S batteries with high performance, Nano Res 6 (2013) 38–46, https://doi.org/10.1007/s12274-012-0279-1.

[15] A. Jain, S.P. Ong, G. Hautier, W. Chen, W.D. Richards, S. Dacek, S. Cholia, D. Gunter, D. Skinner, G. Ceder, K.A. Persson, Commentary: the materials project: a materials genome approach to accelerating materials innovation, APL Mater. 1 (2013), 011002, https://doi.org/10.1063/1.4812323.

[16] K. Saravanan, Y. Basdogan, J. Dean, J.A. Keith, Computational investigation of CO_2 electroreduction on tin oxide and predictions of Ti, V, Nb and Zr dopants for improved, Catal., J. Mater. Chem. A 5 (2017) 11756–11763, https://doi.org/10.1039/C7TA00405B.

[17] J. Oviedo, M.J. Gillan, Energetics and structure of stoichiometric SnO₂ surfaces studied by first-principles calculations, Surf. Sci. 463 (2000) 93–101, https://doi.org/10.1016/S0039-6028(00)00612-9.

[18] T.D. Kühne, M. Iannuzzi, M.D. Ben, V.V. Rybkin, P. Seewald, F. Stein, T. Laino, R. Z. Khaliullin, O. Schütt, F. Schiffmann, D. Golze, J. Wilhelm, S. Chulkov, M. H. Bani-Hashemian, V. Weber, U. Borštnik, M. Taillefumier, A.S. Jakobovits, A. Lazzaro, H. Pabst, T. Müller, R. Schade, M. Guidon, S. Andermatt, N. Holmberg, G.K. Schenter, A. Hehn, A. Bussy, F. Belleflamme, G. Tabacchi, A. Glöß, M. Lass, I. Bethune, C.J. Mundy, C. Plessl, M. Watkins, J. VandeVondele, M. Krack, J. Hutter, CP2K: an electronic structure and molecular dynamics software package - quickstep: efficient and accurate electronic structure calculations, J. Chem. Phys. 152 (2020), 194103, https://doi.org/10.1063/5.0007045.

[19] J.P. Perdew, K. Burke, M. Ernzerhof, Generalized gradient approximation made simple, Phys. Rev. Lett. 77 (1996) 3865–3868, https://doi.org/10.1103/PhysRevLett.77.3865.

[20] D. Wang, R. Cao, S. Hao, C. Liang, G. Chen, P. Chen, Y. Li, X. Zou, Accelerated prediction of cu-based single-atom alloy catalysts for CO₂ reduction by machine learning, Green. Energy Environ. 8 (2023) 820–830, https://doi.org/10.1016/j.gee.2021.10.003.

[21] S. Goedecker, M. Teter, J. Hutter, Separable dual-space gaussian pseudopotentials, Phys. Rev. B 54 (1996) 1703–1710, https://doi.org/10.1103/PhysRevB.54.1703.

[22] S. Grimme, Semiempirical GGA-type density functional constructed with a long-range dispersion correction, J. Comput. Chem. 27 (2006) 1787–1799, https://doi.org/10.1002/jcc.20495.

[23] A.A. Peterson, F. Abild-Pedersen, F. Studt, J. Rossmeisl, J.K. Nørskov, How copper catalyzes the electroreduction of carbon dioxide into hydrocarbon fuels, Energy Environ. Sci. 3 (2010) 1311–1315, https://doi.org/10.1039/C0EE00071J.

[24] Q. Tang, Y. Lee, D.-Y. Li, W. Choi, C.W. Liu, D. Lee, D.-e. Jiang, Lattice-hydride mechanism in electrocatalytic CO₂ Reduction by Structurally Precise Copper-Hydride Nanoclusters, J. Am. Chem. Soc. 139 (2017) 9728–9736, https://doi.org/10.1021/jacs.7b05591.

[25] J.K. Nørskov, J. Rossmeisl, A. Logadottir, L. Lindqvist, J.R. Kitchin, T. Bligaard, H. Jónsson, Origin of the overpotential for oxygen reduction at a fuel-cell cathode, J. Phys. Chem. B 108 (2004) 17886–17892, https://doi.org/10.1021/jp047349j.

[26] S. Li, D. Alfonso, A.V. Nagarajan, S.D. House, J.C. Yang, D.R. Kauffman, G. Mpourmpakis, R. Jin, Monopalladium substitution in gold nanoclusters enhances CO₂ electroreduction activity and selectivity, ACS Catal. 10 (2020) 12011–12016, https://doi.org/10.1021/acscatal.0c02266.

[27] S. Li, A.V. Nagarajan, D.R. Alfonso, M. Sun, D.R. Kauffman, G. Mpourmpakis, R. Jin, Boosting CO₂ electrochemical reduction with atomically precise surface modification on gold nanoclusters, Angew. Chem. Int. Ed. 60 (2021) 6351–6356, https://doi.org/10.1002/anie.202016129.

[28] L. Farsi, N.A. Deskins, First principles analysis of surface dependent segregation in bimetallic alloys, Phys. Chem. Chem. Phys. 21 (2019) 23626–23637, https://doi.org/10.1039/C9CP03984H.

[29] R.G. Musket, Y.E. Strausser, Detection of monolayer quantities of oxygen on silicon using energy-dispersive x-ray spectrometry, Appl. Phys. Lett. 37 (1980) 478–480, https://doi.org/10.1063/1.91737.

[30] E.A. Stefaniak, A. Worobiec, S. Potgieter-Vermaak, A. Alsecz, S. Török, R. Van Grieken, Molecular and elemental characterisation of mineral particles by means of parallel micro-raman spectrometry and scanning electron microscopy/energy dispersive x-ray analysis, Spectrochim. Acta B 61 (2006) 824–830, https://doi.org/10.1016/j.sab.2006.04.009.

[31] X. Liang, C. Hart, Q. Pang, A. Garsuch, T. Weiss, L.F. Nazar, A highly efficient polysulfide mediator for lithium–sulfur batteries, Nat. Commun. 6 (2015) 5682, https://doi.org/10.1038/ncomms6682.

[32] P.M. Shanthi, P.J. Hanumantha, K. Ramalinga, B. Gattu, M.K. Datta, P.N. Kumta, Sulfonic acid based complex framework materials (CFM): nanostructured polysulfide immobilization systems for rechargeable lithium–sulfur battery, J. Electrochem. Soc. 166 (2019) A1827–A1835, https://doi.org/10.1149/2.0251910jes.

[33] M. Fantauzzi, B. Elsener, D. Atzei, A. Rigoldi, A. Rossi, Exploiting XPS for the identification of sulfides and polysulfides, RSC Adv. 5 (2015) 75953–75963, https://doi.org/10.1039/C5RA14915K.

[34] L.G. Devi, R. Kavitha, Enhanced photocatalytic activity of sulfur doped TiO₂ for the decomposition of phenol: a new insight into the bulk and surface modification, Mater. Chem. Phys. 143 (2014) 1300–1308, https://doi.org/10.1016/j.matchemphys.2013.11.038.

[35] K. Ben Mabrouk, T.H. Kauffmann, H. Aroui, M.D. Fontana, Raman study of cation effect on sulfate vibration modes in solid state and in aqueous solutions, J. Raman Spectrosc. 44 (2013) 1603–1608, https://doi.org/10.1002/jrs.4374.

[36] A. Dutta, A. Kuzume, M. Rahaman, S. Vesztergom, P. Broekmann, Monitoring the chemical state of catalysts for CO₂ electroreduction: an in operando study, ACS Catal. 5 (2015) 7498–7502, https://doi.org/10.1021/acscatal.5b02322.

[37] A. Dutta, A. Kuzume, V. Kaliginedi, M. Rahaman, I. Sinev, M. Ahmadi, B. Roldán Cuenya, S. Vesztergom, P. Broekmann, Probing the chemical state of tin oxide NP catalysts during CO₂ electroreduction: a complementary operando approach, Nano Energy 53 (2018) 828–840, https://doi.org/10.1016/j.nanoen.2018.09.033.

[38] X. Zhang, Y. Zhou, H. Zhang, H. Li, K. Liu, H. Li, H. Pan, J. Hu, J. Fu, S. Chen, M. Liu, Tuning the electron structure enables the NiZn alloy for CO₂ electroreduction to formate, J. Energy Chem. 63 (2021) 625–632, https://doi.org/10.1016/j.jechem.2021.08.060.

[39] B. Ren, G. Wen, R. Gao, D. Luo, Z. Zhang, W. Qiu, Q. Ma, X. Wang, Y. Cui, L. Ricardez–Sandoval, A. Yu, Z. Chen, Nano-crumples induced sn-bi bimetallic interface pattern with moderate electron bank for highly efficient CO₂ electroreduction, Nat. Commun. 13 (2022) 2486, https://doi.org/10.1038/s41467-022-29861-w.

[40] X. Zhang, Y. Li, Review of two-dimensional materials for electrochemical CO₂ reduction from a theoretical perspective, Wiley Interdiscip. Rev. Comput. Mol. Sci. 9 (2019), e1416, https://doi.org/10.1002/wcms.1416.

[41] M. Ramdin, A.R.T. Morrison, M. de Groen, R. van Haperen, R. de Kler, E. Irtem, A. T. Laitinen, L.J.P. van den Broeke, T. Breugelmans, J.P.M. Trusler, Wd Jong, T.J. H. Vlugt, High-pressure electrochemical reduction of CO₂ to formic acid/formate: effect of ph on the downstream separation process and economics, Ind. Eng. Chem. Res. 58 (2019) 22718–22740, https://doi.org/10.1021/acs.iecr.9b03970.

[42] M. Oßkopp, A. Löwe, C.M.S. Lobo, S. Baranyai, T. Khoza, M. Auinger, E. Klemm, Producing formic acid at low pH values by electrochemical CO₂ reduction, J. CO₂ Util. 56 (2022), 101823, https://doi.org/10.1016/j.jcou.2021.101823.

[43] G. Wen, B. Ren, X. Wang, D. Luo, H. Dou, Y. Zheng, R. Gao, J. Gostick, A. Yu, Z. Chen, Continuous CO₂ electrolysis using a CO₂ exsolution-induced flow cell, Nat. Energy 7 (2022) 978–988, https://doi.org/10.1038/s41560-022-01130-6.

[44] L. Fan, C. Xia, P. Zhu, Y. Lu, H. Wang, Electrochemical CO₂ reduction to high-concentration pure formic acid solutions in an all-solid-state reactor, Nat. Commun. 11 (2020) 3633, https://doi.org/10.1038/s41467-020-17403-1.

[45] Q. Cheng, C. Hu, G. Wang, Z. Zou, H. Yang, L. Dai, Carbon-defect-driven electroless deposition of Pt atomic clusters for highly efficient hydrogen evolution, J. Am. Chem. Soc. 142 (2020) 5594–5601, https://doi.org/10.1021/jacs.9b11524.